Anisotropic acoustic phonon polariton-enhanced infrared spectroscopy for single molecule detection†

Wei Lyu,[a,b,c] Hanchao Teng,[b,c] Chenchen Wu,[b,c] Xiaotao Zhang,[a] Xiangdong Guo,*[b,c] Xiaoxia Yang*[b,c] and Qing Dai *[b,c]

Nanoscale Fourier transform infrared spectroscopy (nano-FTIR) based on scanning probe microscopy enables the identification of the chemical composition and structure of surface species with a high spatial resolution (~10 nm), which is crucial for exploring catalytic reaction processes, cellular processes, virus detection, *etc*. However, the characterization of a single molecule with nano-FTIR is still challenging due to the weak coupling between the molecule and infrared light due to a large size mismatch. Here, we propose a novel structure (monolayer α-MoO_3/air nanogap/Au) to excite anisotropic acoustic phonon polaritons (APhPs) with ultra-high field confinement (mode volume, $V_{APhPs} \sim 10^{-11}V_0$) and electromagnetic energy enhancement (>10^7), which largely enhance the interaction of single molecules with infrared light. In addition, the anisotropic APhP-assisted nano-FTIR can detect single molecular dipoles in directions both along and perpendicular to the probe axis, while pristine nano-FTIR mainly detects molecular dipoles along the probe axis. The proposed structure provides a way to detect a single molecule, which will impact the fields of biology, chemistry, energy, and environment through fundamental research and applications.

Introduction

The ability to characterize the chemical composition and structure of a single molecule is essential in DNA sequencing,[1,2] cellular processes,[3,4] molecular dynamic process,[5,6] and virus detection.[7] Fourier transform infrared spectroscopy (FTIR) can realize fast and non-destructive identification of molecular fingerprint information and is widely used in biomolecular detection,[8,9] biological processes monitoring[10,11] and pollutant detection.[12] More importantly, the development of nano-FTIR based on scanning probe microscopy (SPM) such as scattering scanning near-field optical microscopy (s-SNOM), photothermal-induced resonance microscopy, peak force infrared microscopy, and photo-induced force microscopy can break the optical diffraction limit (>4 μm for FTIR) and provide high spatial resolution (~10 nm) for single molecule detection.[13] For example, nano-FTIR has been recently used to detect the fingerprint spectra of polydimethylsiloxane (PDMS) nanoparticles[14] and protein particles.[15] However, the infrared spectra of a single molecule is still too weak to be detected by nano-FTIR, which is limited by weak light–matter interaction between infrared light (whose wavelength is ~10 μm scale) and a single molecule (whose wavelength is always <10 nm) due to their large size mismatch. Although the scanning probe has a lightning rod effect to enhance the strength of the electromagnetic field, nano-FTIR working in the tapping mode has an amplitude modulation in the order of tens of nanometers,[16–18] making it difficult to meet the electromagnetic energy enhancement (>10^5) required for single molecule detection.[19] Moreover, the dipole of the s-SNOM tip is mainly along the tip axis (*z*-direction),[20,21] and it would result in low dipole–dipole coupling efficiency to the molecular dipole along the substrate plane (*x*–*y*-direction).

Highly confined two-dimensional (2D) polaritons, such as graphene plasmons,[22,23] and h-BN phonon polaritons (PhPs),[24–27] can compress the light wavelength from the micro-scale to nanoscale,[28] and can largely enhance the infrared absorption of molecules.[29–31] For example, graphene plasmons have been used to enhance the infrared spectra of 8 nm PEO

[a]*Tianjin Key Laboratory of Molecular Optoelectronic Sciences, Department of Chemistry, School of Science, Tianjin University, Tianjin 300072, China*
[b]*CAS Key Laboratory of Nanophotonic Materials and Devices, CAS Key Laboratory of Standardization and Measurement for Nanotechnology, CAS Center for Excellence in Nanoscience, National Center for Nanoscience and Technology, Beijing 100190, China*
[c]*Center of Materials Science and Optoelectronics Engineering, University of Chinese Academy of Sciences, Beijing 100049, China.*
E-mail: daiq@nanoctr.cn, yangxx@nanoctr.cn, guoxd@nanoctr.cn;
Tel: +86-010-82545720
†Electronic supplementary information (ESI) available. See DOI: 10.1039/d1nr01701b

film,[32] 0.8 nm silk protein film,[19] trace SO_2, NO_2, N_2O gas,[33] *etc*. The hyperbolic property endows h-BN PhPs with higher wavelength compression and field enhancement, which can detect a 3 nm thick 4,4′-bis(*N*-carbazolyl)-1,1′-biphenyl (CBP) film.[31] Hyperbolic α-MoO_3 with in-plane anisotropic PhPs, is expected to have even higher electromagnetic field enhancement than h-BN PhPs, especially for the monolayer α-MoO_3 which theoretically has the highest wavelength compression compared to multilayer α-MoO_3.[34–41] In addition, a resonance structure design can further enhance the electromagnetic field of the polaritons, such as acoustic graphene plasmons and acoustic h-BN PhPs formed in nanocavities.[42–45]

Here, we constructed a monolayer α-MoO_3/0.6 nm gap/Au heterostructure to excite highly confined anisotropic APhPs in α-MoO_3 to detect a single molecule by using s-SNOM. The APhPs have extremely high electromagnetic energy enhancement (>10^7), which can greatly enhance the light–matter interaction. Moreover, the APhP-enhanced nano-FTIR can detect molecules with the polarization direction perpendicular to the tip axis (in the *x*–*y* plane), while the pristine nano-FTIR only detects molecular polarization along the tip axis. In addition, the in-plane anisotropy coupling efficiency of the APhPs to the molecule dipole with different polarization (varied nearly 20 fold) can be used as a probe for recognizing the in-plane dipole orientation of a single molecule. Our combination of s-SNOM and α-MoO_3 APhPs provides a theoretical demonstration for the efficient detection of a single molecule.

Results and discussion

The detection of a single molecule by using anisotropic APhPs in the designed α-MoO_3/air nanogap/Au heterostructure is schematically shown in Fig. 1a. s-SNOM is used to excite hyperbolic PhPs in the monolayer α-MoO_3 and detect the nano-FTIR spectra of the objective molecules. The red and blue arrows represent incident light and scattered light, respectively. A 0.6 nm gap between the monolayer α-MoO_3 and Au substrate is designed to generate acoustic polaritons,[43,45,46] and the objective molecule is placed in the gap for detection.

Firstly, we numerically simulate the electric field distribution of the APhPs in the α-MoO_3/Au heterostructure using the commercial software package COMSOL. In the simulation, the thickness of the α-MoO_3 monolayer is modeled as 0.7 nm.[47] According to continuum electrodynamics for 2D phonon polaritons, the monolayer material does not have significant *z*-axis polarizability,[48,49] thus we take a constant ε_z = 6.5 for the *z*-axis permittivity of the α-MoO_3 monolayer.[35] The in-plane anisotropic permittivity values ε_x and ε_y are shown in Fig. S1,† which have three Reststrahlen bands (RB_1, RB_2, and RB_3).[50] We mainly focus on RB_2 (821.4–963 cm^{-1}, $\varepsilon_x < 0$, $\varepsilon_y > 0$), while our research results can also apply to RB_1. In RB_2, the freestanding α-MoO_3 monolayer phonon polaritons have significant optical anisotropy and are mainly propagated in the *x*-direction (Fig. 1b). Therefore, we use the cross-section of APhPs propagating along the *x*-direction to analyze the normalized electric field distribution $|\mathrm{Re}(E_z)/\mathrm{Re}(E_{z0})|$as shown in Fig. 1c. For comparison, the same cross section of PhPs propagating in the freestanding α-MoO_3 monolayer is shown in Fig. S2.† The APhPs exhibit a strong capacitor-like (squeezed) electric field in the gap (d = 0.6 nm) between the α-MoO_3 and the Au substrate, while the electric field of PhPs exhibits a vertical symmetry on both sides. Due to the strength of the field squeezing, the maximum nearfield enhancement of the APhPs is about 4-fold greater than that of the PhPs. Importantly, the electromagnetic energy enhancement of APhPs can reach 10^7, which is strong enough to achieve single molecule level detection. Notably, the APhP wavelength (λ_{APhPs} = 10.2 nm, $\lambda_0/\lambda_{\mathrm{APhPs}}$

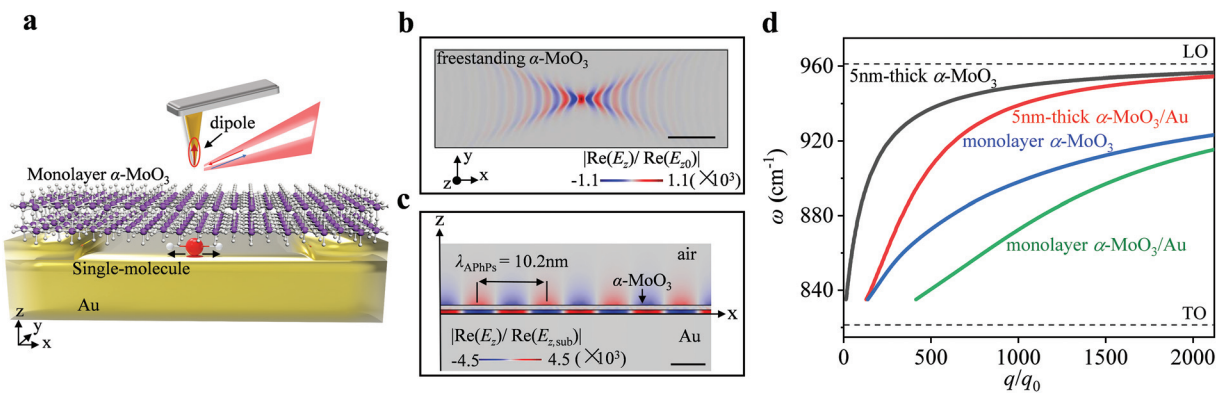

Fig. 1 (a) Schematic diagram of molecular sensing using nano-FTIR with electromagnetic field enhancement of APhPs in the monolayer α-MoO_3/air nanogap/Au heterostructure. The single molecule is located in the air gap between the α-MoO_3 monolayer and the Au substrate. (b) Normalized electric field distribution $|\mathrm{Re}(E_z)/\mathrm{Re}(E_{z0})|$ of freestanding α-MoO_3 monolayer PhPs at ω = 860 cm^{-1}. In RB_2, PhPs propagate in the *x*-direction. Scale bar: 50 nm. (c) Normalized electric field $|\mathrm{Re}(E_z)/\mathrm{Re}(E_{z,\ \mathrm{PhPs}})|$ distribution of APhPs in the monolayer α-MoO_3/0.6 nm air gap/Au heterostructure at ω = 880 cm^{-1}. The APhP wavelength is 10.2 nm. Scale bar: 5 nm. (d) Dispersion curves of the APhPs in monolayer α-MoO_3/0.6 nm air gap/Au (green curve), PhPs on a freestanding monolayer α-MoO_3 (blue curve), APhPs on a 5 nm-thick α-MoO_3/0.6 nm air gap/Au (red curve), and PhPs on a 5 nm-thick freestanding α-MoO_3 layer (black curve). Dashed black lines mark the LO (longitudinal optical phonon) and TO (transverse optical phonon) frequency of the α-MoO_3, respectively.

= 1114) is also shorter than that of the PhPs (λ_{PhPs} = 18.8 nm, λ_0/λ_{PhPs} = 604), which has a larger light wavelength confinement than the corresponding graphene[46] and h-BN[45] acoustic polariton modes.

The dispersion relationship of APhPs in the α-MoO_3/air nanogap/Au heterostructure is calculated *via* both the Fresnel reflection coefficient $r_p(q, \omega)$ method (Fig. S3†) and the finite element method (FEM). The data obtained from these two calculation methods are in excellent agreement (Fig. S4†). For comparison, we also calculated the dispersion of PhPs in the freestanding α-MoO_3 monolayer, a 5 nm thick α-MoO_3 layer, and the α-MoO_3 (5 nm thick)/0.6 nm air gap/Au heterostructure, respectively (Fig. 1d). As shown, the wavevectors for the APhP modes (q_{APhPs}) are larger than those of the PhPs (q_{PhPs}) at each frequency, and the monolayer α-MoO_3 APhPs have the largest wavevectors (Fig. 1d).

For the ultra-high wavelength compression of APhPs ($\lambda_0/\lambda_{APhPs} \sim 10^3$) in this monolayer α-$MoO_3$/nanogap/Au heterostructure, we consider the nonlocal effect.[51,52] There are two nonlocal effects: the nonlocal response of 2D materials and the nonlocal response of the Au substrate. For 2D phononic materials, only when the q_{APhPs} is comparable to the inverse of the out-of-plane atomic layer spacing (or that of the in-plane lattice distance), the effective permittivity needs to be modified by the nonlocal effect.[50] In this case, since $1/a > 10^4 q_0$ and $q_{APhPs} \sim 10^3 q_0$, nonlocal effects in the monolayer α-MoO_3 can be ignored in our calculations. Then we consider the nonlocal Au in our calculations by replacing Au with a composite material, comprising a thin dielectric layer on top of local Au.[53] In Fig. 2a, we compared the APhP dispersion curves of the same monolayer α-MoO_3/air nanogap/Au heterostructures using local and nonlocal Au in the calculation, respectively. As shown, the solid dots (nonlocal Au) can repeat the solid curve (local Au) well, implying the nonlocal effect of Au can also be ignored. Our calculations demonstrate that even when d is as small as 0.3 nm (*i.e.*, 1 atom thick), this nonlocal effect can also be ignored in our α-MoO_3/Au heterostructure.

To optimize the electromagnetic field enhancement, we studied the effects of air gap distances in the monolayer α-MoO_3/air nanogap/Au heterostructure. In Fig. 2b, the plot of q_{APhPs} as a function of d for a fixed frequency ω = 880 cm^{-1} through theoretical calculations of r_p (red solid curve) and the FEM (blue triangle), which are consistent. As d increases from 0.3 nm (*i.e.*, one atom thick) to 4 nm, q_{APhPs} rapidly decreases because the coupling between the polaritons in the monolayer α-MoO_3 and the Au substrate becomes weaker as the gap distance d increases, as displayed in the inset of Fig. 2b. When d is further increased to 8 nm (purple dot), q_{APhPs} becomes nearly the same as q_{PhPs} (black dashed curve), indicating that the coupling between the polariton and the Au substrate vanishes. Thus, the smaller the gap distance d between the monolayer α-MoO_3 and the Au substrate (valid for local Au), the higher the confinement.

When d is 0.3 nm, the APhP wavelength, *i.e.*, $\lambda_{APhPs} = \lambda_0/1475$ (for λ_0 = 11.36 μm) can be compressed more than 10^3-fold. This corresponds to a mode volume of V_{APhPs} = 18 nm^3 ($V_{APhPs} = \lambda_{APhPs}^2 \times d$) and a mode volume ratio of $V_{APhPs}/V_0 \approx 1.2 \times 10^{-11}$ where $V_0 = \lambda_0^3$. The group velocities[54] of APhP are calculated from the dispersion curves using $V_g = \partial\omega/\partial q$, as shown in Fig. 2c. The V_g of APhP in the α-MoO_3/0.6 nm air gap/Au heterostructure can reach~$c/10^5$ (c is the velocity of light in free space), which is much smaller than that in the α-MoO_3 monolayer ($V_g \sim c/38\,000$, black curve). These ultra-confined electromagnetic modes as well as the low group velocity imply strong light–matter interaction, which is significant for single molecule detection.

We chose the α-MoO_3/0.6 nm air gap/Au heterostructure to detect a single molecule using nano-FTIR because the 0.6 nm air gap can provide ultrahigh electromagnetic field enhancement as stated above, and is suitable to hold a single mole-

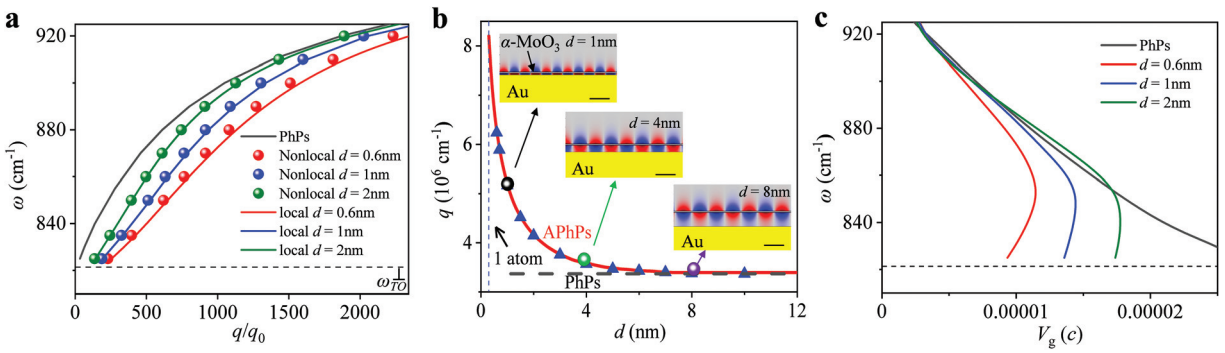

Fig. 2 (a) Dispersion curves of APhPs in monolayer α-MoO_3/air nanogap/Au with different gap distances, d = 2 nm (green dots/curve), d = 1 nm (blue dots/curve) and d = 0.6 nm (red dots/curve), which are calculated by considering nonlocal/local Au. The black curve shows the dispersion of PhPs on a freestanding α-MoO_3 monolayer. (b) The wavevector of APhPs as a function of gap-distance dependent on monolayer α-MoO_3/air nanogap/Au. The red curve is the imaginary part of the calculated Fresnel reflection coefficient, and the blue triangle is obtained by FEM simulation. The black dashed curve shows the PhP wavevector for a freestanding α-MoO_3 monolayer. Inset: electric field distribution of APhPs with d = 1, 4, and 8 nm. Scale bar: 5 nm. (c) Calculated group velocities of APhPs in monolayer α-MoO_3/air nanogap/Au with d = 2 nm (green curve), d = 1 nm (blue curve), d = 0.6 nm (red curve), and PhPs in freestanding α-MoO_3 monolayer (black solid curve). Black dashed curves in (a) and (c) mark the TO phonon frequency of α-MoO_3.

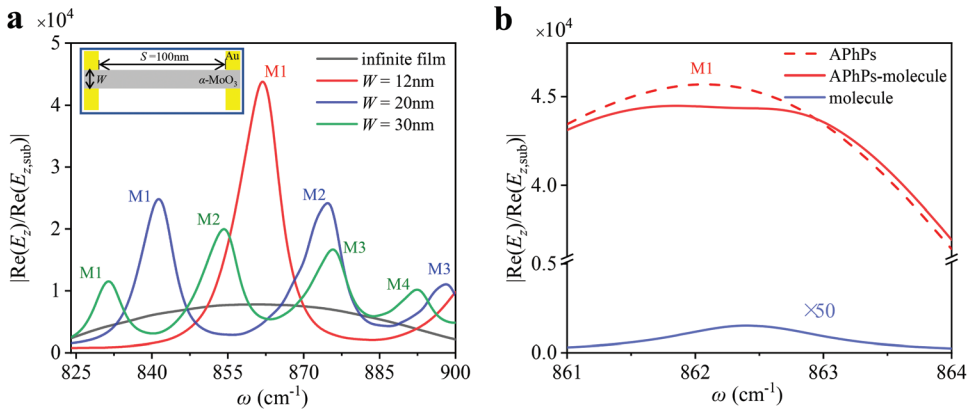

Fig. 3 (a) Normalized electric-field spectra $|\mathrm{Re}(E_z)/\mathrm{Re}(E_{z,\,sub})|$ of APhPs in α-MoO_3 nanoribbon/0.6 nm air gap/Au. There are three different α-MoO_3 nanoribbon widths, *i.e.*, 12 nm (red curve), 20 nm (blue curve), and 30 nm (green curve). The ribbon length is fixed to be 100 nm. M1–M4 represent the multi-order modes of the APhP resonance peak. Inset: Top view of the α-MoO_3 nanoribbon/air nanogap/Au structure. (b) Normalized electric-field spectra $|\mathrm{Re}(E_z)/\mathrm{Re}(E_{z,\,sub})|$ of APhPs coupling with a single molecule (red solid curve). The pristine electric-field spectrum of the APhPs is shown as the dashed red curve. The spectrum of the bare molecule signal is amplified by 50 fold (blue solid curve).

cule. The nano-FTIR is simplified as a vertical electric dipole light source in our model since the tip-scattered signal of nano-FTIR can be qualitatively approximated by simulating a vertical electric field $|\mathrm{Re}(E_z)|$ below a dipole source placed above the sample.[17,21] First, we calculated the pristine spectra, *i.e.*, $|\mathrm{Re}(E_z)/\mathrm{Re}(E_{z,\,sub})|$ as a function of the frequency, of the monolayer α-MoO_3/0.6 nm air gap/Au structure and monolayer α-MoO_3 nanoribbon/0.6 nm air gap/Au structures as shown in Fig. 3a. The α-MoO_3 nanoribbons have a width of 12, 20, and 30 nm in the *x*-direction, and a length of 100 nm in the *y*-direction (Fig. 3a, inset). By cutting the monolayer α-MoO_3 into nanoribbons in the heterostructure, the APhP resonance peak splits into four peaks (marked by M1–M4). They can be assigned to the 1st, 2nd, 3rd, and 4th order of the nanocavity APhPs from the electric field distributions of M1–M4 (Fig. S5 and S6, details in the ESI†). As the α-MoO_3 ribbon width

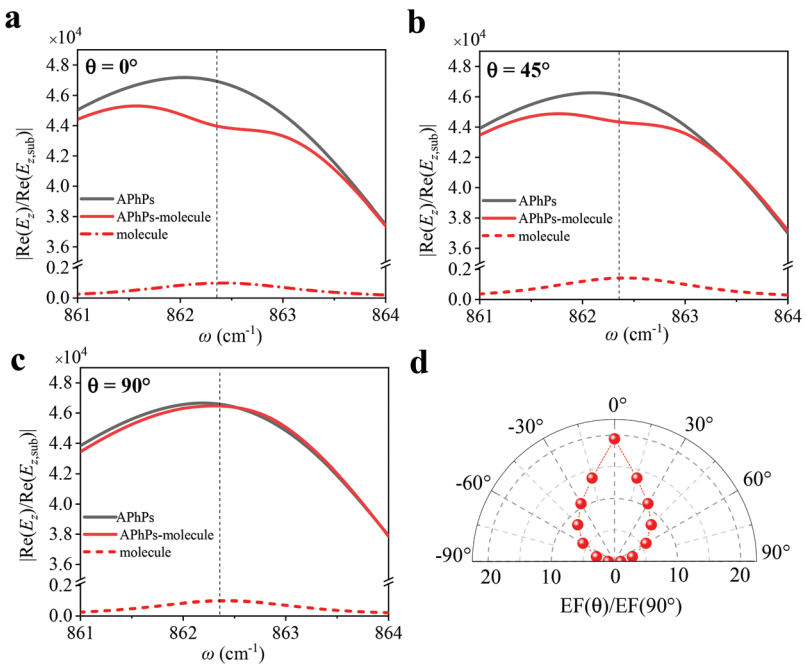

Fig. 4 Normalized electric-field spectra $|\mathrm{Re}(E_z)/\mathrm{Re}(E_{z,\,sub})|$ of APhPs with the molecule (red curves) when the angle between the molecular dipole and the APhP polarization is θ = 0° (a), θ = 45° (b), θ = 90° (c). The bare molecule signal spectrum is displayed as a red dashed curve and the pristine APhP spectrum is displayed as the black curve in (a–c). Inset of (a–c): Schematic diagram of the angle θ between the orientation of the molecular dipole and the propagation direction of APhPs. (d) The enhancement factor of APhPs to molecular signal EF as a function of θ, which is normalized by EF(90°).

becomes smaller, the electromagnetic field of the APhPs becomes stronger, and the corresponding frequency blue shifts. The normalized electric field strength $|\mathrm{Re}(E_z)/\mathrm{Re}(E_{z,\,\mathrm{sub}})|$ maximum of 12 nm wide α-MoO_3 nanoribbon APhPs is about 5 times larger than that of the α-MoO_3 film (black curve), and the electromagnetic energy enhancement can reach 10^8. We use it to detect a single molecule with the size of 5 × 5 × 0.6 nm. The molecule is put in the 0.6 nm air gap, where the hot spot is located (Fig. S7†). A molecular vibration mode at 863 cm^{-1} is used as an example whose permittivity is plotted in Fig. S8.† The molecule spectrum (blue solid curve in Fig. 3b) is too weak to be directly distinguished, and we enlarged it by 50-fold for viewing. After combining with the APhPs, the molecular signal appears as an obvious Fano dip in the broad APhP resonance spectrum, and the enhancement can be calculated to be about 45-fold. In contrast, the signal enhancement of the same molecule monolayer *via* the α-MoO_3/0.6 nm air gap/Au structure is about 3-fold (details in Fig. S9†). The Fano dip feature originates from the destructive interference between the molecular vibration mode and the APhP resonance mode, and the APhPs are the strongly absorption active modes, while the weakly absorbing molecular vibration that is coupled to APhPs is the passive (dark) mode.

At last, we take advantage of the anisotropic α-MoO_3 APhPs to identify the in-plane dipole orientations of a single molecule. We set an in-plane dipole and studied the single molecule detected by nano-FTIR as a function of the angle (θ) between the molecular dipole and the α-MoO_3 APhPs. Due to the weak coupling between nano-FTIR and the in-plane dipole, we set the intensity of this in-plane dipole to be 200 times that of the single molecule used above. When θ changes from θ = 0° to θ = 90° (Fig. 4), the dip feature in the APhP resonance spectrum decreases until it disappears. More APhP resonance spectra (θ = 15°, 30°, 60° and 75°) can be found in Fig. S10.† We calculated the enhancement effect EF of APhPs on molecular signals at different angles θ (Fig. 4d). We obtained molecular resonance spectra following APhP enhancement by subtracting the APhP resonance spectrum with the molecule from the APhP resonance spectrum without the molecule. And the result is then divided by the original signal of the molecule to obtain the enhancement factor EF.[32] The EF is the smallest when the molecular vibration dipole is completely perpendicular to the APhP propagation direction (*i.e.*, θ = 90°). The molecular signal enhancement effect of θ = 0° is 20 times than that of θ = 90°. Therefore, anisotropic APhPs can not only enhance the single molecule signal, but also can be used as probes to identify the in-plane vibrational dipole orientation of the single molecule.

Conclusions

In summary, we designed a monolayer α-MoO_3/0.6 nm gap/Au heterostructure to excite highly confined anisotropic APhPs by using s-SNOM. APhPs have a ultra-high mode volume ($\sim 10^{-11} V_0$) and ultra-slow group velocity ($V_g \sim c/10^5$), which can enhance the single molecule detection efficiency (~45-fold). In addition, due to the in-plane optical anisotropy of APhPs, the coupling efficiency between α-MoO_3 APhPs and the single-molecule dipole with different orientations has a huge difference of nearly 20 times, which can realize the recognition of a single molecule in in-plane dipole orientation. Therefore, combining the APhPs in the α-MoO_3/Au heterostructure and s-SNOM has demonstrated significant application advantages in the field of single molecular optical sensing, laying a theoretical foundation for future single molecule infrared fingerprint detection.

Methods

Full wave simulations

This work is based on the finite element method (FEM) of the simulation software COMSOL. We used a 2D boundary transmission model to calculate the field distribution of APhPs/PhPs in Fig. 1 The largest mesh size of the α-MoO_3 area is 0.2 nm, for which the calculations reached proper convergence, while we used a 3D model with the scattering boundary condition as shown in Fig. 3 and 4. The vertically electric dipole source is 5 nm above the α-MoO_3 monolayer. The largest mesh size for the α-MoO_3 area is 1 nm. The value of the z component of the electric field $|\mathrm{Re}(E_z)|$ is taken from 0.3 nm above the α-MoO_3. $|\mathrm{Re}(E_z)/\mathrm{Re}(E_{z,\,\mathrm{sub}})|$ indicates the electric field enhancement, where $|\mathrm{Re}(E_{z,\,\mathrm{sub}})|$ is the electric field above the Au substrate. The electric field distribution interface is taken from 0.1 nm below the α-MoO_3.

Molecule permittivity model

In our model, the vibrational mode of a given molecule is modeled by the following Lorentz oscillator: $\varepsilon(\omega) = \varepsilon_\infty + f \times (\omega_n^2 - \omega^2 - i\omega\Gamma)^{-1}$, where f = 15.8 cm^{-2} represents the molecular signal oscillation intensity, ω is the infrared incident frequency, ε_∞ = 1 represents the constant dielectric background, ω_n = 863 cm^{-1} represents the molecular vibrational frequency, and Γ = 1.3 cm^{-1} represents the molecular damping constant.

Conflicts of interest

The authors declare no competing financial interest.

Acknowledgements

This work was supported by the National Key R&D Program of China (2016YFA0300903), the National Natural Science Foundation of China (51925203, 52022025, 51972074, 11674073, and U2032206), the Key Program of the Bureau of Frontier Sciences and Education, Chinese Academy of Sciences (QYZDB-SSW-SLH021), the Strategic Priority Research Program of the Chinese Academy of Sciences (XDB30000000 and XDB36000000), the Key Research Program of the Chinese Academy of Sciences (ZDBS-SSW-JSC002), Youth Innovation

Promotion Association CAS, and CAS Interdisciplinary Innovation Team (JCTD-2018-03).

Notes and references

1 M. Taniguchi, *ACS Omega*, 2020, **5**, 959–964.
2 C. Jia, B. Ma, N. Xinand and X. Guo, *Acc. Chem. Res.*, 2015, **48**, 2565–2575.
3 S. Mohapatra, C.-T. Lin, X. A. Feng, A. Basuand and T. Ha, *Chem. Rev.*, 2020, **120**, 36–78.
4 Y. Zhang, R.-n. Huaand and C.-y. Zhang, *Anal. Chem.*, 2020, **92**, 4700–4706.
5 Y. Li, L. Zhao, Y. Yaoand and X. Guo, *ACS Appl. Bio Mater.*, 2020, **3**, 68–85.
6 J. Guan, C. Jia, Y. Li, Z. Liu, J. Wang, Z. Yang, C. Gu, D. Su, K. N. Houk, D. Zhangand and X. Guo, *Sci. Adv.*, 2018, **4**, eaar2177.
7 A. M. Shrivastav, U. Cvelbarand and I. Abdulhalim, *Commun. Biol.*, 2021, **4**, 70.
8 F. Neubrech, C. Huck, K. Weber, A. Pucciand and H. Giessen, *Chem. Rev.*, 2017, **117**, 5110–5145.
9 X. Yang, Z. Sun, T. Low, H. Hu, X. Guo, F. J. García de Abajo, P. Avourisand and Q. Dai, *Adv. Mater.*, 2018, **30**, 1704896.
10 M. A. Fallah, C. Stanglmair, C. Pacholskiand and K. Hauser, *Langmuir*, 2016, **32**, 7356–7364.
11 D. Rodrigo, A. Tittl, N. Ait-Bouziad, A. John-Herpin, O. Limaj, C. Kelly, D. Yoo, N. J. Wittenberg, S.-H. Oh, H. A. Lashueland and H. Altug, *Nat. Commun.*, 2018, **9**, 2160.
12 M. Hassan, E. Gonzalez, V. Hitchinsand and I. Ilev, *Sens. Actuators, B*, 2016, **231**, 646–654.
13 C. Luo, X. Guo, H. Hu, D. Hu, C. Wu, X. Yangand and Q. Dai, *Adv. Opt. Mater.*, 2020, **8**, 1901416.
14 F. Huth, A. Govyadinov, S. Amarie, W. Nuansing, F. Keilmannand and R. Hillenbrand, *Nano Lett.*, 2012, **12**, 3973–3978.
15 F. S. Ruggeri, B. Mannini, R. Schmid, M. Vendruscoloand and T. P. J. Knowles, *Nat. Commun.*, 2020, **11**, 2945.
16 D. Hu, X. Yang, C. Li, R. Liu, Z. Yao, H. Hu, S. N. G. Corder, J. Chen, Z. Sun, M. Liuand and Q. Dai, *Nat. Commun.*, 2017, **8**, 1471.
17 P. Li, I. Dolado, F. J. Alfaro-Mozaz, A. Y. Nikitin, F. Casanova, L. E. Hueso, S. Vélezand and R. Hillenbrand, *Nano Lett.*, 2017, **17**, 228–235.
18 F. J. Alfaro-Mozaz, P. Alonso-González, S. Vélez, I. Dolado, M. Autore, S. Mastel, F. Casanova, L. E. Hueso, P. Li, A. Y. Nikitinand and R. Hillenbrand, *Nat. Commun.*, 2017, **8**, 15624.
19 I.-H. Lee, D. Yoo, P. Avouris, T. Lowand and S.-H. Oh, *Nat. Nanotechnol.*, 2019, **14**, 313–319.
20 Y. Luan, L. McDermott, F. Huand and Z. Fei, *Phys. Rev. Appl.*, 2020, **13**, 034020.
21 A. Y. Nikitin, P. Alonso-González, S. Vélez, S. Mastel, A. Centeno, A. Pesquera, A. Zurutuza, F. Casanova, L. E. Hueso, F. H. L. Koppensand and R. Hillenbrand, *Nat. Photonics*, 2016, **10**, 239–243.
22 A. N. Grigorenko, M. Poliniand and K. S. Novoselov, *Nat. Photonics*, 2012, **6**, 749–758.
23 F. H. L. Koppens, D. E. Changand and F. J. García de Abajo, *Nano Lett.*, 2011, **11**, 3370–3377.
24 P. N. Li, I. Dolado, F. J. Alfaro-Mozaz, F. Casanova, L. E. Hueso, S. Liu, J. H. Edgar, A. Y. Nikitin, S. Velezand and R. Hillenbrand, *Science*, 2018, **359**, 892–896.
25 S. Y. Dai, M. Tymchenko, Y. F. Yang, Q. Ma, M. Pita-Vidal, K. Watanabe, T. Taniguchi, P. Jarillo-Herrero, M. M. Fogler, A. Aluand and D. N. Basov, *Adv. Mater.*, 2018, **30**, 1706358.
26 S. Dai, Z. Fei, Q. Ma, A. S. Rodin, M. Wagner, A. S. McLeod, M. K. Liu, W. Gannett, W. Regan, K. Watanabe, T. Taniguchi, M. Thiemens, G. Dominguez, A. H. Castro Neto, A. Zettl, F. Keilmann, P. Jarillo-Herrero, M. M. Foglerand and D. N. Basov, *Science*, 2014, **343**, 1125–1129.
27 J. D. Caldwell, A. V. Kretinin, Y. G. Chen, V. Giannini, M. M. Fogler, Y. Francescato, C. T. Ellis, J. G. Tischler, C. R. Woods, A. J. Giles, M. Hong, K. Watanabe, T. Taniguchi, S. A. Maierand and K. S. Novoselov, *Nat. Commun.*, 2014, **5**, 5221.
28 D. K. Gramotnevand and S. I. Bozhevolnyi, *Nat. Photonics*, 2010, **4**, 83–91.
29 A. Bylinkin, M. Schnell, M. Autore, F. Calavalle, P. Li, J. Taboada-Gutièrrez, S. Liu, J. H. Edgar, F. Casanova, L. E. Hueso, P. Alonso-Gonzalez, A. Y. Nikitinand and R. Hillenbrand, *Nat. Photonics*, 2020, **15**, 197–202.
30 D. Rodrigo, O. Limaj, D. Janner, D. Etezadi, F. J. García de Abajo, V. Pruneriand and H. Altug, *Science*, 2015, **349**, 165–168.
31 M. Autore, P. Li, I. Dolado, F. J. Alfaro-Mozaz, R. Esteban, A. Atxabal, F. Casanova, L. E. Hueso, P. Alonso-González, J. Aizpurua, A. Y. Nikitin, S. Vélezand and R. Hillenbrand, *Light: Sci. Appl.*, 2018, **7**, 17172.
32 H. Hu, X. Yang, F. Zhai, D. Hu, R. Liu, K. Liu, Z. Sunand and Q. Dai, *Nat. Commun.*, 2016, **7**, 12334.
33 H. Hu, X. Yang, X. Guo, K. Khaliji, S. R. Biswas, F. J. García de Abajo, T. Low, Z. Sunand and Q. Dai, *Nat. Commun.*, 2019, **10**, 1131.
34 W. Dong, R. Qi, T. Liu, Y. Li, N. Li, Z. Hua, Z. Gao, S. Zhang, K. Liu, J. Guoand and P. Gao, *Adv. Mater.*, 2020, **32**, 2002014.
35 G. Alvarez-Perez, T. G. Folland, I. Errea, J. Taboada-Gutierrez, J. Duan, J. Martin-Sanchez, A. I. F. Tresguerres-Mata, J. R. Matson, A. Bylinkin, M. He, W. Ma, Q. Bao, J. I. Martin, J. D. Caldwell, A. Y. Nikitinand and P. Alonso-Gonzalez, *Adv. Mater.*, 2020, **32**, e1908176.
36 Z. Zheng, N. Xu, S. L. Oscurato, M. Tamagnone, F. Sun, Y. Jiang, Y. Ke, J. Chen, W. Huang, W. L. Wilson, A. Ambrosio, S. Dengand and H. Chen, *Sci. Adv.*, 2019, **5**, eaav8690.
37 Z. Zheng, F. Sun, W. Huang, J. Jiang, R. Zhan, Y. Ke, H. Chenand and S. Deng, *Nano Lett.*, 2020, **20**, 5301–5308.
38 G. Hu, Q. Ou, G. Si, Y. Wu, J. Wu, Z. Dai, A. Krasnok, Y. Mazor, Q. Zhang, Q. Bao, C.-W. Qiuand and A. Alù, *Nature*, 2020, **582**, 209–213.

39 M. Chen, X. Lin, T. H. Dinh, Z. Zheng, J. Shen, Q. Ma, H. Chen, P. Jarillo-Herreroand and S. Dai, *Nat. Mater.*, 2020, **19**, 1307–1311.

40 J. Duan, N. Capote-Robayna, J. Taboada-Gutiérrez, G. Álvarez-Pérez, I. Prieto, J. Martín-Sánchez, A. Y. Nikitinand and P. Alonso-González, *Nano Lett.*, 2020, **20**, 5323–5329.

41 W. Ma, P. Alonso-Gonzalez, S. Li, A. Y. Nikitin, J. Yuan, J. Martin-Sanchez, J. Taboada-Gutierrez, I. Amenabar, P. Li, S. Velez, C. Tollan, Z. Dai, Y. Zhang, S. Sriram, K. Kalantar-Zadeh, S. T. Lee, R. Hillenbrandand and Q. Bao, *Nature*, 2018, **562**, 557–562.

42 D. Alcaraz Iranzo, S. Nanot, E. J. C. Dias, I. Epstein, C. Peng, D. K. Efetov, M. B. Lundeberg, R. Parret, J. Osmond, J. Y. Hong, J. Kong, D. R. Englund, N. M. R. Peresand and F. H. L. Koppens, *Science*, 2018, **360**, 291–295.

43 P. Alonso-González, A. Y. Nikitin, Y. Gao, A. Woessner, M. B. Lundeberg, A. Principi, N. Forcellini, W. Yan, S. Vélez, A. J. Huber, K. Watanabe, T. Taniguchi, F. Casanova, L. E. Hueso, M. Polini, J. Hone, F. H. L. Koppensand and R. Hillenbrand, *Nat. Nanotechnol.*, 2017, **12**, 31–35.

44 S. G. Menabde, I. H. Lee, S. Lee, H. Ha, J. T. Heiden, D. Yoo, T. T. Kim, T. Low, Y. H. Lee, S. H. Ohand and M. S. Jang, *Nat. Commun.*, 2021, **12**, 938.

45 Z. Yuan, R. Chen, P. Li, A. Y. Nikitin, R. Hillenbrandand and X. Zhang, *ACS Photonics*, 2020, **7**, 2610–2617.

46 S. Chen, M. Autore, J. Li, P. N. Li, P. Alonso-Gonzalez, Z. L. Yang, L. Martin-Moreno, R. Hillenbrandand and A. Y. Nikitin, *ACS Photonics*, 2017, **4**, 3089–3097.

47 Y. Du, G. Li, E. W. Peterson, J. Zhou, X. Zhang, R. Mu, Z. Dohnálek, M. Bowden, I. Lyubinetsky and S. A. Chambers, *Nanoscale*, 2016, **8**, 3119–3124.

48 N. Li, X. Guo, X. Yang, R. Qi, T. Qiao, Y. Li, R. Shi, Y. Li, K. Liu, Z. Xu, L. Liu, F. J. García de Abajo, Q. Dai, E.-G. Wangand and P. Gao, *Nat. Mater.*, 2021, **20**, 43–48.

49 S. Dai, W. Fang, N. Rivera, Y. Stehle, B. Y. Jiang, J. Shen, R. Y. Tay, C. J. Ciccarino, Q. Ma, D. Rodan-Legrain, P. Jarillo-Herrero, E. H. T. Teo, M. M. Fogler, P. Narang, J. Kongand and D. N. Basov, *Adv. Mater.*, 2019, **31**, e1806603.

50 N. Rivera, T. Christensenand and P. Narang, *Nano Lett.*, 2019, **19**, 2653–2660.

51 C. R. Gubbinand and S. De Liberato, *Phys. Rev. X*, 2020, **10**, 021027.

52 M. B. Lundeberg, Y. Gao, R. Asgari, C. Tan, B. Van Duppen, M. Autore, P. Alonso-Gonzalez, A. Woessner, K. Watanabe, T. Taniguchi, R. Hillenbrand, J. Hone, M. Poliniand and F. H. L. Koppens, *Science*, 2017, **357**, 187–191.

53 Y. Luo, A. I. Fernandez-Dominguez, A. Wiener, S. A. Maierand and J. B. Pendry, *Phys. Rev. Lett.*, 2013, **111**, 093901.

54 E. Yoxall, M. Schnell, A. Y. Nikitin, O. Txoperena, A. Woessner, M. B. Lundeberg, F. Casanova, L. E. Hueso, F. H. L. Koppensand and R. Hillenbrand, *Nat. Photonics*, 2015, **9**, 674–678.